



Synergistic photocatalytic inactivation mechanisms of bacteria by graphene sheets grafted plasmonic Ag–AgX (X = Cl, Br, I) composite photocatalyst under visible light irradiation



Dehua Xia^a, Taicheng An^{b, **}, Guiying Li^b, Wanjun Wang^a, Huijun Zhao^c,
Po Keung Wong^{a, *}

^a School of Life Sciences, The Chinese University of Hong Kong, Shatin, NT, Hong Kong Special Administrative Region

^b Institute of Environmental Health and Pollution Control and School of Environmental Science and Engineering, Guangdong University of Technology, Guangzhou 510006, China

^c Centre for Clean Environment and Energy, Gold Coast Campus, Griffith University, Queensland 4222, Australia

ARTICLE INFO

Article history:

Received 28 January 2016

Received in revised form

21 April 2016

Accepted 21 April 2016

Available online 23 April 2016

Keywords:

Ag⁺ ions

Bacterial inactivation

Plasmonic photocatalyst

Synergistic mechanism

Visible light

ABSTRACT

By coupling graphene sheet and plasmonic photocatalysis technologies, a series of Ag–AgX/RGOs (X = Cl, Br, I; RGO = reduced graphene oxide) composites were prepared and found to be efficient antimicrobial agents for water disinfection upon visible light. Attributed to the efficient charge transfer by RGO sheets, the optimum Ag–AgBr/0.5% RGO could completely inactivate 2×10^7 cfu mL⁻¹ of *Escherichia coli* within 8 min, much faster than bare Ag–AgBr within 35 min. The synergistic antimicrobial mechanism of Ag–AgBr/0.5% RGO was studied by Ag⁺ ions release evaluation, radical scavengers study, and radical determination. The enhanced photocatalytic activity of irradiated Ag–AgBr/0.5% RGO originated from the synergistic activities of its three components including Ag, AgBr and RGO, and the proposed mechanisms contained enhanced attraction by RGO followed by two pathways: primary oxidative stress caused by plasma induced reactive species like H₂O₂ and bactericidal effect of released Ag⁺ ions. Furthermore, characterization of *E. coli* cells using SEM, fluorescent microscopy, and cytoplasmic substance leakage illustrated that VL irradiated Ag–AgBr/0.5% RGO could not only cause metabolic dysfunction but also destroy the cell envelope and biomolecular, while irradiated Ag⁺ ions play a differential bactericidal action with a limited metabolic injury and no cell-membrane damage. The present work provides an efficient water disinfection technology and also opens a new idea in studying the antimicrobial mechanism of plasmonic photocatalyst.

© 2016 Elsevier Ltd. All rights reserved.

1. Introduction

Lack of access to safe, reliable water sources remains a critical problem for millions of people worldwide where waterborne diseases such as diarrhea cause up to 1.8 million deaths annually (WHO, 2008). This calls for novel water disinfection technologies that are robust, low-cost, and energy-efficient. Conventional methods of water disinfection such as chlorination, germicidal UV-C exposure, and ozonation are often chemically, energetically or operationally expensive, limited their practical implementation

(Shannon et al., 2008; Qu et al., 2013; Rizzello and Pompa, 2014). Alternatively, semiconductor-mediated photocatalysis has been extensively studied and proposed to be an effective, safe disinfection process, which relies on the *in situ* formation of highly reactive species (RSs) capable of destroying biological water contaminant (Wang et al., 2013b; Xia et al., 2015a). Since then, numerous efficient photocatalysts have been developed and successfully utilized for the photocatalytic inactivation of hazardous microorganisms, which mainly contain two categories: the first involves non-metal/metal doping or anchoring other semiconductors for TiO₂, such as S-doped TiO₂, Fe-doped TiO₂, AgBr/TiO₂, C₃N₄/TiO₂ (Lan et al., 2007; Yao et al., 2007; Yu et al., 2005; Li et al., 2016); and the second is newly developed semiconductors with narrow band-gaps such as Ag–AgI and even non-metal C₃N₄, red phosphorous (Hu et al., 2010; Huang et al., 2014; Xia et al., 2015b), etc. Moreover,

* Corresponding author.

** Corresponding author.

E-mail addresses: antc99@gdut.edu.cn (T. An), pkwong@cuhk.edu.hk (P.K. Wong).

there are still many newly fabricated VLD photocatalysts coming out each year, most of which only focus on the photocatalytic removal of organic pollutants and waste gas (Zhao et al., 2015; Xia et al., 2016), while little work utilized in microorganism inactivation, this motivate us to identify and expand their application for water disinfection.

Among these novel VLD photocatalysts, silver halides (AgX, X = Cl, Br and I) are widely interested by the metallic Ag induced surface plasmon resonance (SPR) effect upon visible light. SPR of Ag nanocrystal could effectively enhance the photocatalytic activity through interaction between free electrons of metal surface and photons (Archana et al., 2015). However, pure AgX nanoparticles are easy to agglomerate and may cause low photocatalytic efficiency (Meng et al., 2013). Therefore, many supports are used to load AgX nanoparticles, carbon material is one of the most promising support, such as activated carbon (AC), carbon nanotube (CNT), and graphene oxide (GO), which could effectively improve the distribution of nanoparticles, electrons transfer, and stability (McEvoy and Zhang, 2014). These carbon based plasmonic photocatalysts like Ag–AgCl/activated carbon, Ag–AgX(Cl, Br, I)/CNT, and Ag–AgX(Cl, Br)/RGO have been well prepared and found to display high efficiency for environmental remediation (Zhu et al., 2011; Shi et al., 2013). Among these materials, Ag–AgX(Cl, Br, I)/RGO is the most efficient one, because the hybridized graphene oxide (GO) with high conductivity could efficiently modify the electronic structure of Ag nanocrystal and extract the excited charge carriers to further enhance the photocatalytic activity of Ag–AgX (Wang et al., 2013a). Moreover, the promoted transportation of charge carriers by GO could also inhibit the reduction of AgX to Ag, leading to better stability of Ag–AgX/RGOs for repetitive use (Luo et al., 2013). These promising results encourage us to utilize plasmonic Ag–AgX/RGOs for water disinfection, as no one has reported the photocatalytic inactivation ability of these composites yet.

Plasmonic photocatalysts like Ag–AgI/Al₂O₃, AgBr–Ag–Bi₂WO₆, Ag–AgX(Cl, Br, I)/CNTs were convinced that all can inactivate bacteria efficiently upon visible light, and the proposed bactericidal effects of these photocatalysts were attributed to the plasmon-induced RSs (reactive species) (Hu et al., 2010; Zhang et al., 2010; Shi et al., 2014). However, the controversy still exist in considering the exact photocatalytic inactivation mechanism of these plasmonic photocatalysts. First, most reports always use “scavenger study” to analyze the roles of plasmon-induced RSs like $\cdot\text{O}_2^-$, H_2O_2 , $\cdot\text{OH}$, but which is an indirect and semi-quantitative tool (Xia et al., 2015a). Meanwhile, “direct determination” with specific probes is more sensitive and can directly quantify the generated reactive species, which can be utilized to compensate the “scavenger study”, thus to double confirm the generated reactive species and analyze their roles more accurately (Xia et al., 2015b). Second, $^1\text{O}_2$ can be generated during photocatalytic process, but its bactericidal role was rarely mentioned in these studies. Actually, $^1\text{O}_2$ possesses a 0.65 eV oxidation potential and can inactivate both Gram positive and Gram negative bacterial cells effectively (Bartusik et al., 2012; Planas et al., 2016). Third, Ag based plasmonic photocatalysts have been reported to release Ag^+ ions during light irradiation, but the potential bactericidal effects from Ag^+ ions are neglected by these reports on the basis of limited cell inactivation with equivalent Ag^+ added. Actually, Ag^+ ions have been well documented which can play multifaceted bactericidal action through destroying biological functional biomolecules such as enzymes, membrane proteins and DNA (Fabrega et al., 2009; Xiu et al., 2014). Thus, it is reasonable to propose that the involved Ag^+ ions may play a synergistic effect with plasmon-induced RSs to inactivate bacteria. These effects pose many challenges in identifying the exact bactericidal mechanism of plasmonic photocatalysts.

In the present study, the Ag–AgX/RGOs were prepared with

modified method in the literature (Zhang et al., 2011), and the as-prepared Ag–AgX/RGOs were firstly employed to inactivate *Escherichia coli* under visible light irradiation. The bactericidal effects of Ag–AgX/RGOs from plasmon-induced RSs and released Ag^+ ions were first analyzed, focusing on the Ag^+ ions release evaluation, radical scavengers study and direct detection of radical with probe. Moreover, in order to build up the current understanding for the exact mechanism of plasmonic photocatalysts in bacterial inactivation, the involved pathways of RSs and/or released Ag^+ ions were systematically investigated and differentiated, in terms of morphological changes, impaired biological action, intracellular reactive oxidants, and leaked cytoplasmic biomolecular during the photocatalytic inactivation. Finally, the synergistic mechanism of the visible-light-mediated antimicrobial activity of Ag–AgX/RGOs toward microbial cells was discussed in detail. Therefore, the present work could not only provide an efficient water disinfection technology but also innovate the understanding of antimicrobial mechanism of plasmonic photocatalyst.

2. Experimental

2.1. Preparation and characterization of Ag–AgX/RGOs

The Ag–AgX/RGOs composites were synthesized with modified method in the literature (Zhang et al., 2011), through deposition-precipitation and followed photo-reduction method. Typically, AgNO_3 (0.21 g) in ammonia (2.3 mL, 25 wt% NH_3) was diluted to 50 mL by deionized water, then graphene oxide (GO) aqueous solution (3.5 mL, with concentration of 100 mg L^{-1}) was added and stirred for 0.5 h. Chemically derived GO carries abundant functional groups, which are leveraged to stabilize Ag ion. Next, KX (X = Cl, Br, I) (1.5 mmol) was added and intensively stirred for 24 h. The above solution was mixed with 50 mL ethanol and irradiated with filtered light ($\lambda > 400 \text{ nm}$) from a 300 W Xenon arc lamp. Under VL irradiation, Ag^+ on the surface of the AgX/GO composites is reduced to Ag^0 species, with the reduction of the adjacent GO to RGO simultaneously. Then the resulting precipitate was centrifuged, washed with deionized water and dried.

X-ray diffractometer (XRD) patterns of as-prepared photocatalysts were obtained on a Shimadzu LabX XRD-6000. The UV–Vis absorption spectra of these photocatalysts were recorded on a Shimadzu UV-2450 spectrophotometer. The transmission electron microscopy (TEM) images for these photocatalysts were performed on a FEI-Tecnai G2 20 and scanning electron microscopy (SEM) images were obtained on a Hitachi S-4800. X-ray photoelectron spectroscopy (XPS) for these photocatalysts was analyzed on a VG ESCALAB 250 spectrometer using a non-monochromatized Al KR X-ray source (1486.6 eV).

2.2. Photocatalytic inactivation process

Escherichia coli K-12 was chosen as a model bacterium to evaluate the photocatalytic inactivation ability of the as-prepared plasmonic photocatalysts. A 50 mL mixture suspension including Ag–AgX/RGOs of 5.0 mg and *E. coli* K-12 of $2 \times 10^7 \text{ cfu mL}^{-1}$ in a flask was put into a photocatalytic reactor and vigorously dispersed by a magnetic stirrer (Fig. S1). Twelve fluorescent tubes (FTs) (15 W, VELOX, Thailand) were installed as light source, and the VL and UV intensities were determined by a light meter (LI-COR, Lincoln, Nebraska, USA), with 9.285 mW cm^{-2} of visible light, 0.065 mW cm^{-2} of UVA, 0.018 mW cm^{-2} of UVB, and $0.0034 \text{ mW cm}^{-2}$ of UVC. Aliquot samples were collected at different time intervals and diluted serially with sterilized saline solution, then immediately spread on the nutrient agar (Lab M, Lancashire, UK) plate for later analysis. All the plates were

incubated at 37 °C for 24 h. Control experiments with light or photocatalyst alone were also conducted in triplicate.

2.3. Analysis method

(i) Scavenger study: Scavenger stock solutions included 1 M isopropanol (Riedel-de Haën, Germany) for $\cdot\text{OH}$, 1 M $\text{K}_2\text{Cr}_2\text{O}_7$ (Merck, Germany) for e^- , 1 M sodium oxalate (Fuchen, China) for h^+ , 100 mM Fe(II)-EDTA for H_2O_2 (prepared with FeSO_4 and Na_2EDTA , Ajax Chemicals, Australia), 100 mM TEMPOL (Fuchen, China) for $\cdot\text{O}_2^-$ and 100 mM L-histidine (Merck, Germany). **(ii) Ag^+ ion release test:** During the inactivation process with Ag–AgBr/0.5% RGO, the harvested samples were captured and filtered through a 0.22 μm filter, then the concentration of released Ag^+ ions was measured by an atomic absorption spectrophotometer (Varian SpectrAA55-B, Palo Alto, USA). Moreover, the equivalent amount of released Ag^+ ions was also mixed with *E. coli* cells to study the inactivation role of Ag^+ ions. **(iii) Extra-cellular reactive species (RSs) assay:** pCBA is a well-known specific probe to detect $\cdot\text{OH}$ due to its high reactivity with $\cdot\text{OH}$ ($k = 5.2 \times 10^9 \text{ M}^{-1} \text{ s}^{-1}$). FFA is extremely reactive toward $^1\text{O}_2$ ($k = 1.2 \times 10^8 \text{ M}^{-1} \text{ s}^{-1}$) and adequately specific for $^1\text{O}_2$. The decay of pCBA and FFA in the collected filtrate was analyzed with a high performance liquid chromatography system (Dionex U3000, Sunnyvale, CA) equipped with a Thermo Scientific Hypersil BDS C18 column. The production of $\cdot\text{O}_2^-$ was quantitatively analyzed by detecting the decrease in the concentration of nitro blue tetrazolium (NBT, $k = 5.88 \times 10^4 \text{ M}^{-1} \text{ s}^{-1}$) at a wavelength of 259 nm with a UV–vis spectrophotometer (LabTech). H_2O_2 was analyzed on a Hitachi F-4500 fluorescence spectrophotometer based on the reaction of H_2O_2 with coumarin to form a high fluorescent compound (7-hydroxycoumarin, 456 nm). All the calculated equations for each species with specific probes are shown in SI. **(iv) Intracellular reactive species (RSs) assay:** The fluorescent probe 2',7'-dichlorodihydrofluorescein diacetate (DCFH-DA) was adopted to monitor the intracellular RSs levels. The non-fluorescent probe DCFH-DA can enter bacterial cells where it can be hydrolyzed by intracellular esterase and further oxidized by intracellular RSs to form fluorescent 2',7'-dichlorofluorescein (DCF). The mechanism and detailed procedures of the fluorescent assay are provided in the supporting information (Fig. S2). **(v) Determination of cellular ATP levels:** *E. coli* cells treated at various times were assayed for adenosine triphosphate (ATP) by a luciferin/luciferase test (BacTiter-Glo Microbial Cell Viability Assay Kit, Promega), and the luminescence signal was measured in a microplate reader (Biotek Synergy 2). **(vi) Leakage of cytoplasmic contents:** The residual protein concentration was measured with the Bradford assay (SK3041, Sangon Biotech, China). The amount of DNA and RNA released from the cytoplasm can be estimated by the detection of the absorbance at 260 nm using UV–vis spectrophotometry (Shimadzu UV-1700). At different time intervals, the harvested bacterial suspensions were filtered through a 0.2 μm syringe filter and then the nucleic acid contents were measured. These tests are according to the method described in the references (Sun et al., 2014).

2.4. Microscopic analysis

(i) Fluorescence images: aliquot samples were collected at different time intervals and subsequently stained with the dye mixture prepared by LIVE/DEAD BacLight Bacterial Viability Kit (L7012, Molecular Probes, Inc., Eugene, OR), then observed under a light microscope (Nikon ECLIPSE 80i, Japan); **(ii) Scanning electron microscopy:** aliquot samples were collected at different time intervals and transferred onto poly-lysine coated cover-slips. The specimen was then post-fixed with 2% osmium tetroxide (E.M.

grade, Electron Microscopy Sciences, Fort Washington, PA, USA), followed by dehydrated in a graded series of ethanol (50, 60, 70, 80, 90, 95 and 100%, and each for 10 min) and critical point dried within CO_2 atmosphere. Finally, the dried specimens were coated with gold and palladium, then observed with a scanning electron microscope (Joel-JSM-6301-F) at an accelerating voltage of 5 kV. Above tests are according to the method described in the references (Xia et al., 2013).

3. Results and discussion

3.1. Structure and properties of Ag–AgX/RGOs

Firstly, the phase structure of the resultant Ag–AgX/RGOs nanocomposites was analyzed by XRD (Fig. 1a). It can be seen that the main characteristic peaks of Ag–AgX/RGOs are matched well with the crystal planes of pure AgX, respectively. Meanwhile, only little diffraction peaks of RGO (002) (JCPDS file, 41-1487) at 26.2° and Ag^0 (JCPDS file, 65-2871) at 37.8° can be observed in these nanocomposites, mainly due to the lower content and high dispersion of Ag^0 and RGO species on these materials. Secondly, XPS tests were conducted to further verify the hybridization structure of Ag–AgX/RGOs, the results in Fig. S3 confirmed the coexistence of C, Ag, X elements in these composites. Moreover, as shown in Fig. 1b, two peaks of Ag species ascribed to $\text{Ag}3d_{5/2}$ and $\text{Ag}3d_{3/2}$ can be further divided, first half bands at 367.5 and 373.5 eV are attributed to Ag^+ , and latter half bands at 368.4 and 374.1 eV are ascribed to the metallic Ag^0 , this confirms the reduction of AgX to Ag^0 after light irradiation. Furthermore, a successful reduction of GO to RGO after light irradiation is also verified, based on the diminished C=O, C–O, C(O)O group contents and the increased C/O atomic ratio from 0.52 of pristine GO (Fig. S4) to 1.0458 of Ag–AgBr/RGO, 1.0387 of Ag–AgI/RGO, and 1.0452 of Ag–AgCl/RGO. Thirdly, typical morphologies of the prepared Ag–AgX/RGOs hybrids are shown in Fig. 2, and the EDX results of elemental species and amounts in Table S1 are consistent with XPS analysis. Unlike the smooth AgX particles prepared without GO (Fig. 2a–c), wrinkles AgX nanospheres (average diameter of ca. 1 μm) unwrapped with gauze-like GO nanosheets (Fig. 2d–e), could be obtained in Ag–AgX/RGOs hybrid nanocomposites. It has been reported that the involvement of GO in the AgX growth process could affect the morphology and size of AgX particles (Zhang et al., 2011). Fourthly, the light absorption spectra of as-prepared Ag–AgX/RGOs and bare Ag–AgX samples are shown in Fig. 2g, all of which display strong absorption both in the UV and visible light regions. This is mainly due to the nucleation of Ag^0 species on the surface of AgX, which would arouse strong plasmon resonance absorptions within VL region. Moreover, attributed to the hybrid RGO, Ag–AgX/RGOs photocatalysts exhibit a significant enhancement in VL region than pure Ag–AgX, which may induce higher photocatalytic activity. Fifthly, photoluminescence (PL) was used to analyze the charge transfer ability of Ag–AgX and Ag–AgX/RGO ($X = \text{Cl}, \text{Br}, \text{I}$). As shown in Fig. 2h, the PL intensity of all Ag–AgX/RGOs decreases rapidly compared with that of pure Ag–AgX, indicating that RGO modification could efficiently enhance the separation of charge carriers, this can lead to more generation of RSs and thereby higher photocatalytic activity. In conclusion, the characterization results confirm that all the Ag–AgX/RGOs were successfully synthesized.

3.2. Plasmon-induced photocatalytic performance of Ag–AgX/RGOs

The as-prepared Ag–AgX/RGOs were utilized to evaluate the applicability for water disinfection under visible light irradiation. As shown in Fig. 3a, with light alone, the cell density remained

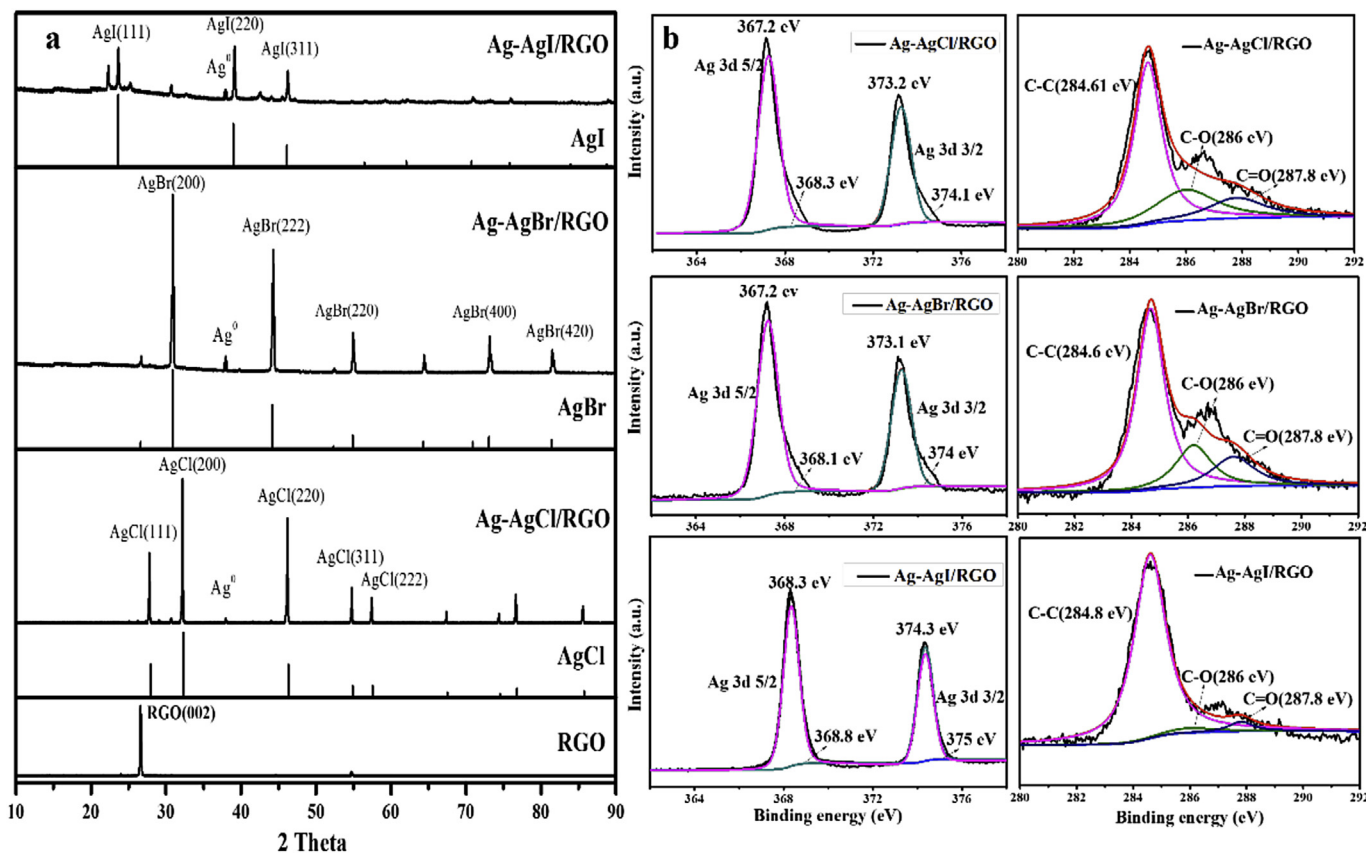


Fig. 1. (a) XRD patterns of Ag–AgX(Cl, Br, I)/RGO, (b) The Ag 3d and C 1s spectra of Ag–AgX/RGO (X = Cl, Br, I).

essentially unchanged, indicating that only visible-light irradiation had no bactericidal effect on the bacterial cells. Meanwhile, after mixing with multiple types of Ag–AgX/RGOs in dark for 40 min, the bacterial population remained almost constant with only about $0.03\text{--}0.1 \log_{10} \text{ cfu mL}^{-1}$ cells' loss (Fig. 3a and b), indicating no serious toxic effect caused by the photocatalysts alone. Fig. 3c shows the photocatalytic inactivation kinetics with different Ag–AgX/RGOs upon visible light irradiation. Obviously, Ag–AgBr/RGO exhibited the highest photocatalytic inactivation efficiency and obtained complete inactivation of about $7 \log \text{ cfu mL}^{-1}$ *E. coli* cells within 8 min, much faster than those of Ag–AgCl/RGO within 25 min and Ag–AgI/RGO within 35 min. This is mainly attributed to the smaller band gap of AgBr (2.69 eV) than that of AgCl (2.90 eV) and AgI (2.88 eV), thereby the Ag–AgBr/RGO could be more readily excited by a wide range of visible light (Shi et al., 2014). However, the optimum Ag–AgBr/RGO is still not as efficient as the bio-synthesized Ag nanoparticles, as which can obtain total inactivation of $6 \log_{10} \text{ cfu mL}^{-1}$ *E. coli* K-12 within 1 min (Xi et al., 2014).

Since Ag–AgBr/RGO exhibited the highest photocatalytic performance in Ag–AgX/RGOs, thus Ag–AgBr/RGO with different weight ratio of Ag–AgBr:RGO were prepared to search for the optimum one. As shown in Fig. 3d, the best inactivation performance with total inactivation of $7 \log_{10} \text{ cfu mL}^{-1}$ was obtained over Ag–AgBr/0.5% RGO within 8 min, much faster than that of bare Ag–AgBr (one way ANOVA, $p < 0.05$), inferring that hybrid graphene sheets could significantly enhance the photocatalytic activity of pure Ag–AgBr (one way ANOVA, $p < 0.05$). Obviously, with the increase of hybrid RGO ratio from 0.1 to 0.5 wt%, Ag–AgBr/RGO exhibited an obviously enhanced photocatalytic performance (one way ANOVA, $p < 0.05$). This can be ascribed to the enhanced light absorption and the accelerated electron transfer by the RGO,

leaving more separated e^- and h^+ to form reactive species and thus inducing a higher photocatalytic performance (Li et al., 2013). However, when the hybrid ratio of RGO further increased from 1 to 2 wt%, a clear deterioration of the photocatalytic performance was observed (one way ANOVA, $p < 0.05$). This is mainly caused by the “shielding effect”, even if light adsorption and electron-transfer process were further enhanced by excessive RGO, the introduction of a large amount of black graphene sheet would cover the active sites on the Ag–AgBr surface and also compete the light adsorption with Ag–AgBr, leading to a worse photocatalytic performance than pure Ag–AgBr (Lin et al., 2011). Therefore, an appropriate RGO percentage in nanocomposites is critical for improving the resultant photocatalytic activity. The following work will be focused on using the optimum Ag–AgBr/0.5% RGO for bacterial inactivation.

3.3. Synergistic photocatalytic inactivation mechanism of Ag–AgBr/0.5% RGO

Obviously, Ag–AgBr/0.5% RGO exhibits excellent antimicrobial activities under VL irradiation. The antimicrobial ability of Ag–AgBr/0.5% RGO should originate from the synergistic activities of its three components, i.e., RGO, Ag and AgBr nanoparticles. Therefore, the corresponding activities of three components of Ag–AgBr/0.5% RGO upon visible light were studied in order to reveal the synergistic antimicrobial mechanism of Ag–AgBr/0.5% RGO. As shown in Fig. 4a, pure RGO did not show any antimicrobial activities against *E. coli* cells upon visible light, indicating its negligible bactericidal role. Meanwhile, pure AgBr exhibited antimicrobial activities with $4 \log \text{ cfu mL}^{-1}$ cells' loss within 40 min mainly due to its VLD photocatalytic activities. After Ag

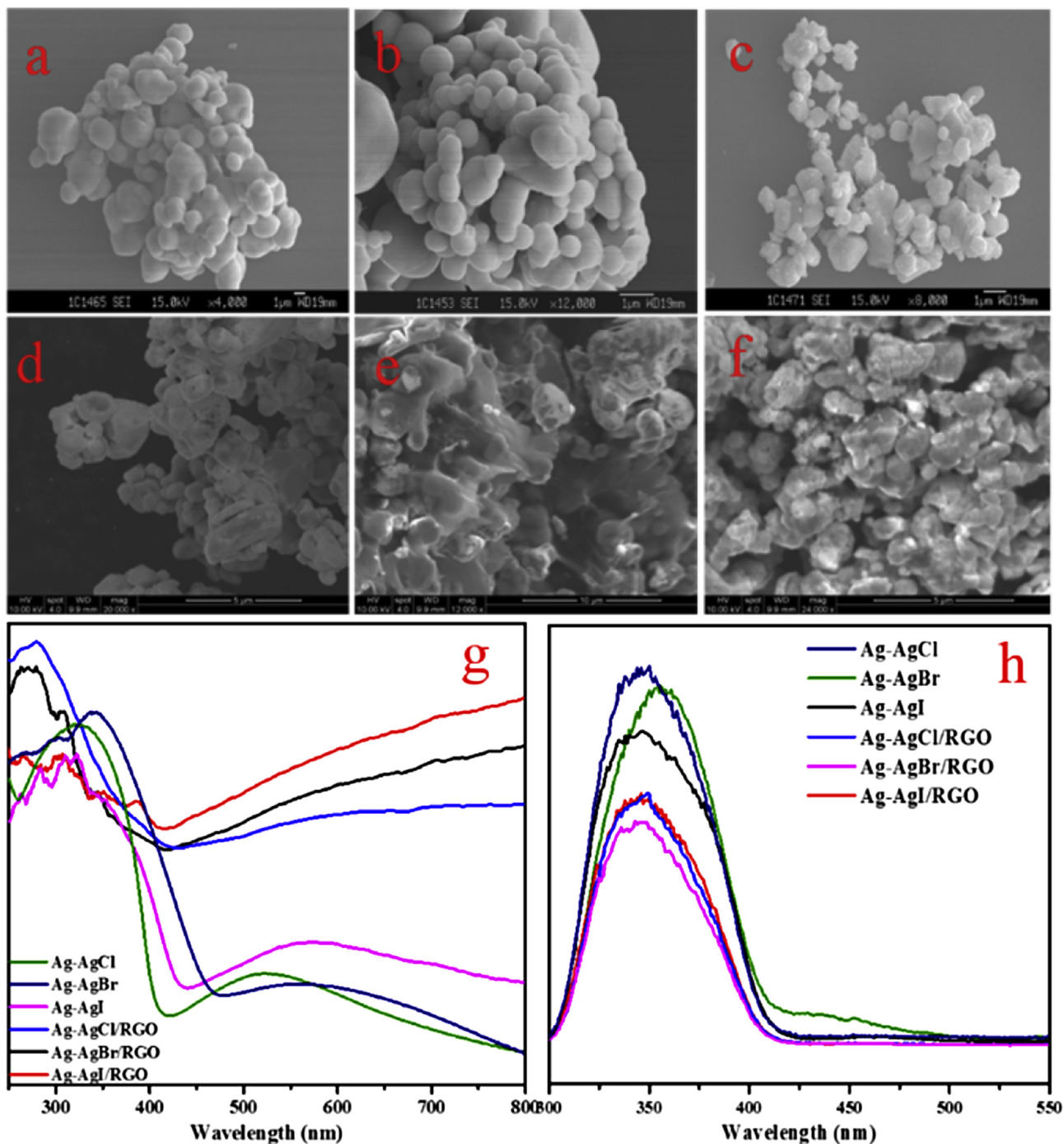


Fig. 2. SEM images of (a) Ag–AgCl, (b) Ag–AgBr, (c) Ag–AgI, (d) Ag–AgCl/RGO, (e) Ag–AgBr/RGO, (f) Ag–AgI/RGO; (g) UV–Vis diffused reflectance spectra of Ag–AgX(Cl, Br, I)/RGO; (h) photoluminescence intensity of Ag–AgX/RGOs.

nanoparticles loading, the antimicrobial activity of both Ag–RGO and Ag–AgBr was enhanced obviously though still lower than that of Ag–AgBr/0.5% RGO. The obvious difference of antimicrobial activity between pure RGO and Ag–RGO illustrated that Ag nanoparticles could contribute to inactivate microbial cells independently, while the enhanced activity of Ag–AgBr compared with pure AgBr may originate from the plasmon-induced photocatalytic effect. Moreover, to differentiate the bactericidal role of Ag nanoparticles formed on the surface of AgBr, the equivalent amount of Ag nanoparticles (0.006 g L^{-1} , quantified through XPS analysis in

Fig. S5 and Table S2) were also utilized for bacterial inactivation. Obviously, Ag nanoparticles alone exhibited limited inactivation of $0.45 \log_{10} \text{ cfu mL}^{-1}$ of cell loss within same time period. In contrast with the inactivation efficiency of Ag–AgBr and AgBr, that of Ag nanoparticles is much lower. Therefore, the primary contribution to the enhanced photocatalytic performance of Ag–AgBr can be attributed to the plasmonic effect of Ag nanoparticles. Similar observation was also obtained by Hu et al. (2010). Obviously, it can be found that the three components of Ag–AgBr/0.5% RGO collectively contribute to the enhanced photocatalytic performance.

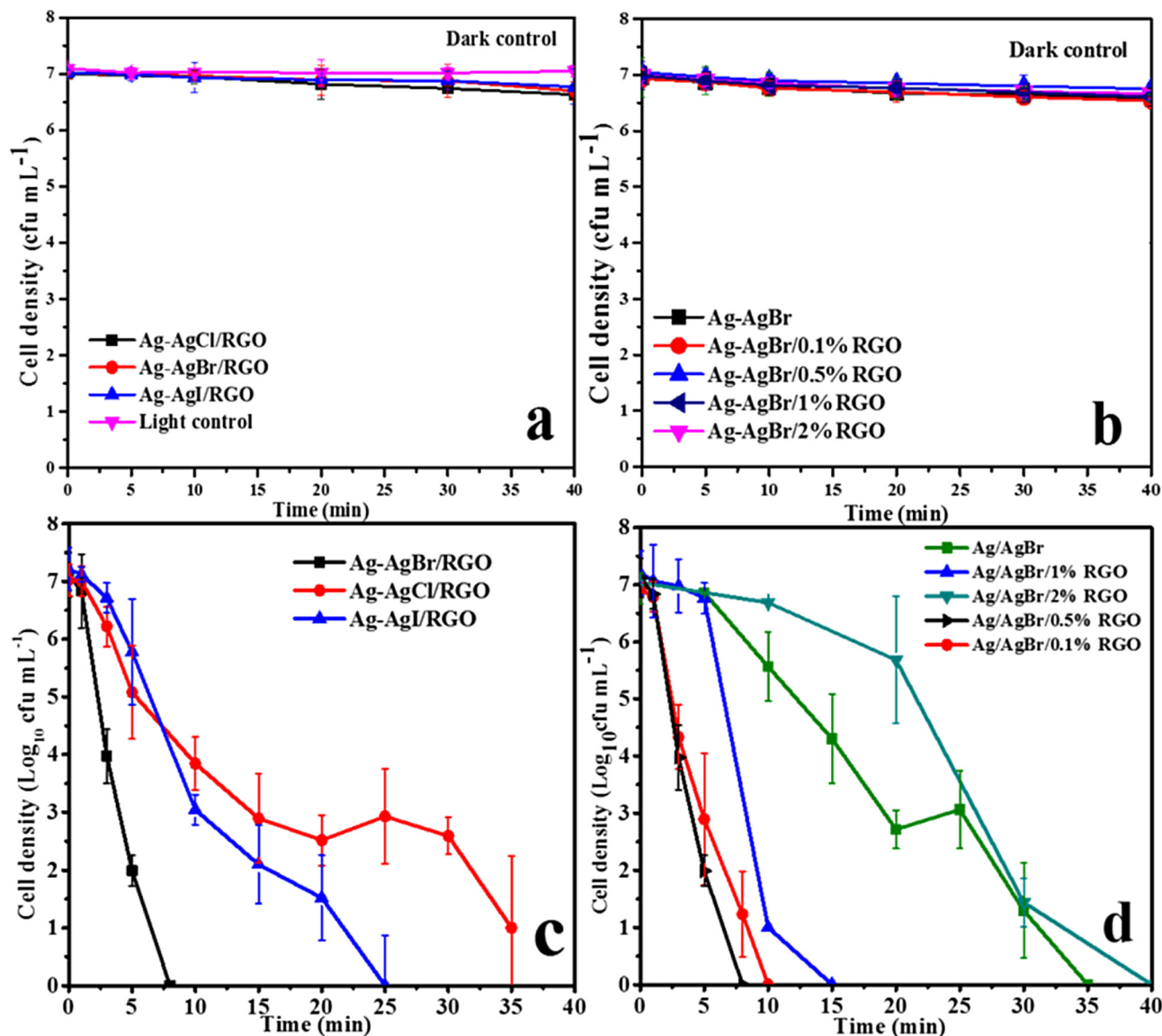


Fig. 3. *E. coli* K-12 inactivation curves with (a) Ag–AgX(Cl, Br, I)/RGO and (b) Ag–AgBr/RGO with different weight of RGO in dark; photocatalytic inactivation curves of *E. coli* K-12 with (c) Ag–AgX(Cl, Br, I)/RGO and (d) Ag–AgBr/RGO with different weight of RGO under fluorescent tubes irradiation. Experimental conditions: [*E. coli* K-12] = 2×10^7 cfu mL^{-1} , [Ag–AgX/RGOs] = 0.1 g L^{-1} .

It is generally accepted that Ag^+ ions at high concentrations exhibits bactericidal activity, thus the contribution of Ag^+ ions for the antimicrobial activity of Ag–AgBr/0.5% RGO was also studied. First, upon light irradiation and dark condition, Ag^+ ions released from Ag–AgBr/0.5% RGO in saline solution alone (as control) and the mixture solution of *E. coli* cells and saline were evaluated. As shown in Fig. 4b, the concentration of Ag^+ ions was found to increase gradually in both solutions, and Ag^+ ions in the mixture solution of *E. coli* cells and saline (light- 0.58 mg L^{-1} , dark- 0.3 mg L^{-1}) was higher than in the saline alone (light- 0.34 mg L^{-1} , dark- 0.23 mg L^{-1}), illustrating that released Ag^+ ions could bind to the outer surface or penetrate into the cells, to further trigger the release of Ag^+ ions. Meanwhile, it was also found that Ag^+ ions released under light irradiation (mixture solution- 0.58 mg L^{-1} , saline- 0.30 mg L^{-1}) was much higher than in the dark (mixture solution- 0.34 mg L^{-1} , saline- 0.23 mg L^{-1}), inferring that light can significantly promote the photo-corrosion of Ag nanoparticles. In contrast with other Ag/Ag₂S nanoparticles (Pang et al., 2010) and

Ag/TiO₂/SiO₂ films (Xi et al., 2014) with barely Ag^+ release, Ag–AgBr/RGO with more Ag^+ leakage is mainly due to its well mixture with bacterial cells in saline solution, which could trigger Ag^+ release by uptaking by cells and forming insoluble AgCl. Second, the bactericidal ability of released Ag^+ ions at concentration of 0.58 mg L^{-1} was also evaluated to make a comparison. As shown in Fig. 4b, there are about $0.3 \text{ log}_{10} \text{ cfu mL}^{-1}$ cells' loss within 40 min light irradiation and only $0.07 \text{ log}_{10} \text{ cfu mL}^{-1}$ cells' loss in dark, suggesting the Ag^+ ions play a more serious bactericidal effect under light irradiation (one-way ANOVA, $p < 0.05$). This is mainly due to the alteration in the physiology of bacterial cells after light irradiation, including increases the bacterial intracellular Fe^{2+} level and favors hydroxyl radical ($\cdot\text{OH}$) production, thus to increase bacterial susceptibility and accelerate bacterial inactivation (Ng et al., 2015). Meanwhile, it can be found that the inactivation curves with Ag^+ ions in dark control ($0.07 \text{ log}_{10} \text{ cfu mL}^{-1}$ cells' loss) are almost consistent with that of Ag–AgBr/0.5% RGO during dark control experiments (Fig. 3b), indicating cells' loss after mixture

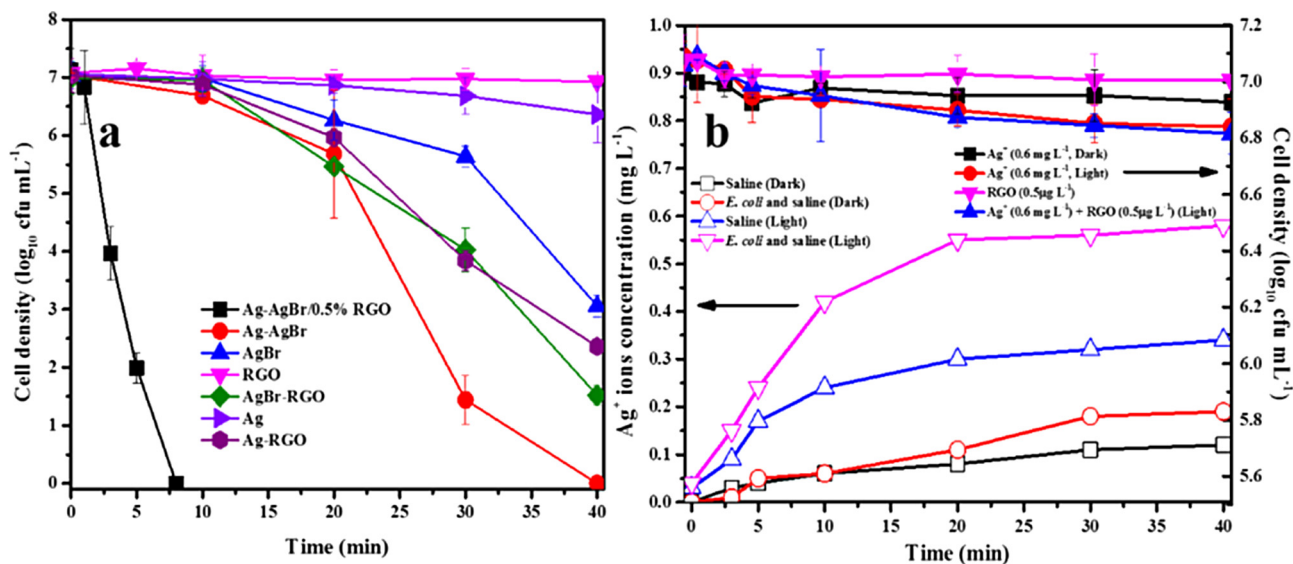


Fig. 4. (a) Antimicrobial activities of the different components of Ag–AgBr/0.5% RGO against *E. coli* K-12 under fluorescent tubes irradiation; (b) Ag ions release into mixture of *E. coli* cells and saline with Ag–AgBr/0.5% RGO; and inactivation curves with released Ag⁺ ions, RGO and mixture of Ag⁺ ions and RGO. Experimental conditions: [*E. coli* K-12] = 2×10^7 cfu mL⁻¹, [Ag–AgBr/0.5% RGO] = 0.1 g L⁻¹.

with Ag–AgBr/0.5% RGO in dark is due to the released Ag⁺ ions. Moreover, when $0.5 \mu\text{g mL}^{-1}$ RGO was added into Ag⁺ ions solution, the inactivation efficiency were in similar pattern without any enhancement, further illustrating the independent bactericidal role of Ag⁺ ions with negligible contribution of RGO. In conclusion, these results reveal that Ag⁺ ions play a role in the bacterial inactivation, while light irradiation can promote the release of free Ag⁺ ions from Ag–AgBr/0.5% RGO and also enhance the antimicrobial activities of Ag⁺ ions.

Since the released Ag⁺ ions can only cause limited bacterial inactivation ($0.3 \log_{10}$ cfu mL⁻¹ cells' loss), the primary bactericidal effect of VL irradiated Ag–AgBr/0.5% RGO should result from its sustainable generated reactive species (RSs). Therefore, the bactericidal role of plasma-induced RSs from irradiated Ag–AgBr/0.5% RGO were analyzed through scavenger studies and also directly determined with specific probe simultaneously. Generally, $7 \log_{10}$ cfu mL⁻¹ of *E. coli* cells could be completely inactivated within 10 min when no scavenger added. First, among the reactive oxygen species (ROSSs, i.e. $^1\text{O}_2$, $^{\bullet}\text{O}_2^-$, H_2O_2 , $^{\bullet}\text{OH}$), hydroxyl radical ($^{\bullet}\text{OH}$) was found to play the lowest bactericidal role, the inactivation kinetics was inhibited with survival of $3 \log_{10}$ cfu mL⁻¹ *E. coli* cells in the presence of isopropanol ($^{\bullet}\text{OH}$ scavenger) within same experimental period (Fig. 5a). Meanwhile, the involvement of $^{\bullet}\text{OH}$ was confirmed by the increasing fluorescence intensities emitted at 440 nm of terephthalic acid (Fig. S6) and the steady-state $^{\bullet}\text{OH}$ concentration ($[\text{OH}]_{\text{ss}}$) measured using pCBA was approximately 2.858×10^{-14} M (Fig. 5b). Second, $^1\text{O}_2$ was found to have a moderate bactericidal role (Fig. 5a), the inactivation kinetics was inhibited with residual of $4 \log_{10}$ cfu mL⁻¹ cells in the presence of L-histidine (1 mM, $^1\text{O}_2$ scavenger) over the experimental period. Similarly, the formation of $^1\text{O}_2$ was also evidenced by the fact that 30% degradation of FFA (100 μM , a probe for $^1\text{O}_2$) was obtained and the $[\text{O}_2]_{\text{ss}}$ was 1.2384×10^{-12} M (Fig. 5c). Third, it can be found that the bacterial inactivation was greatly depressed by TEMPOL ($^{\bullet}\text{O}_2^-$ scavenger) with residual of $6 \log_{10}$ cfu mL⁻¹ *E. coli* cells within 10 min (Fig. 5a), indicating a more significant inactivation effect of $^{\bullet}\text{O}_2^-$ than $^1\text{O}_2$ and $^{\bullet}\text{OH}$. Similarly, nitroblue tetrazolium (NBT, 0.15 mM, a probe for $^{\bullet}\text{O}_2^-$), as indicated by the observation of great decrease in the absorption at 260 nm upon light irradiation,

confirming the large formation of $^{\bullet}\text{O}_2^-$ and $[\text{O}_2^-]_{\text{ss}}$ is 1.14×10^{-8} M (Fig. 5d). Fourth, it is noteworthy to find the critical involvement of H_2O_2 for bacterial inactivation, affirmed by the almost total inhibition of *E. coli* cells' loss after adding Fe(II)-EDTA (Fig. 5a). The accumulated concentration of H_2O_2 in the present system was attained to almost 2.33 μM after light irradiation (Fig. 5e). Fortunately, the results of "direct determination" indicate that the sequence of the concentrations of RS is $[\text{H}_2\text{O}_2]_{\text{ss}} > [\text{O}_2^-]_{\text{ss}} > [\text{O}_2]_{\text{ss}} > [\text{OH}]_{\text{ss}}$, which is consistent with the results in the scavenger study. These results indicate that H_2O_2 is the primary ROSSs generated from Ag–AgBr/0.5% RGO, collectively work with other ROSSs like $^{\bullet}\text{OH}$, $^1\text{O}_2$ and $^{\bullet}\text{O}_2^-$ to take part in the photocatalytic inactivation.

As the precursors of derivative ROSSs, both photogenerated h^+ and e^- are found to be significantly involved in the photocatalytic process, evidenced by the great inhibition in inactivation after respective addition of oxalate (h^+ scavenger) and Cr(IV) (e^- scavenger) in Ag–AgBr/0.5% RGO suspension. Especially, the leading bactericidal role of e^- rather than h^+ is expected, mainly due to the plasmon-induced electron transfer process as illustrated in Fig. 6. Under VL irradiation, the electrons and holes can be produced from AgBr, and Ag nanoparticles are also excited to generate electron–hole pairs due to the localized SPR (Eqs. (1) and (2)) (Kuai et al., 2010). The excited electrons in the conduction band of AgBr can quickly transfer toward Ag nanoparticles, due to the high conductivity and the storing electrons capacity of the Ag nanoparticles. Meanwhile, the electrons in the conduction band of AgBr may also transfer to the surface of RGO, which can facilitate the fast and long-range interfacial charge transfer along the π - π graphitic carbon network owing to its superior conductivity. Additionally, the electrons generated from Ag nanoparticles could also flow to RGO (Zhu et al., 2012). Therefore, both plasmon-excited Ag nanoparticles and RGO could serve as electron transfer media in the vectorial electron transfers of AgBr \rightarrow RGO and/or AgBr \rightarrow Ag \rightarrow RGO, thus greatly reducing the recombination possibility with photo generated holes. Therefore, a relative high concentration of electrons with strong reduction potential ($\text{CB}_{\text{AgBr}} = -1.04$ V vs NHE) accumulate onto the surface of RGO, which can readily promote the formation of $^1\text{O}_2$ through energy transfer to O_2 , or directly reduce surface chemisorbed $\text{O}_2/\text{H}_2\text{O}$ to generate $^{\bullet}\text{O}_2^-$ ($E_0(\text{O}_2/\text{O}_2^-) = -0.33$ V vs NHE) (Xia

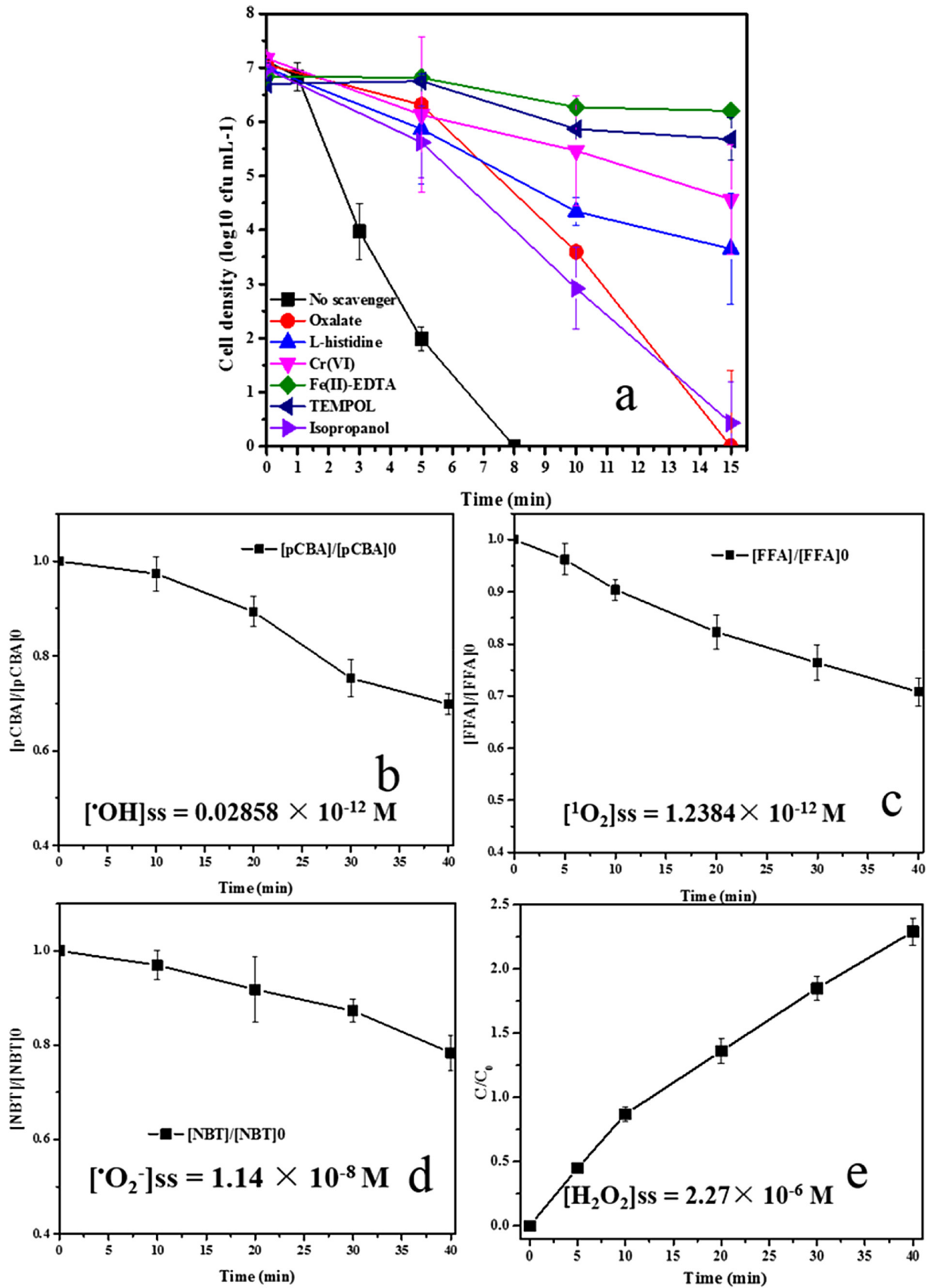
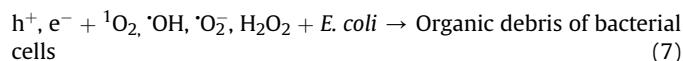
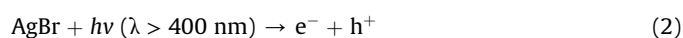


Fig. 5. (a) Photocatalytic inactivation curves in the presence of various scavengers ([Fe-EDTA] = 0.1 mM; [Cr(VI)] = 0.05 mM; [TEMPOL] = 1 mM; [Sodium oxalate] = 0.5 mM; [Isopropanol] = 0.5 mM; [L-histidine] = 0.5 mM); (b) Time-dependent degradation of pCBA to detect $\cdot\text{OH}$ ([pCBA] = 0.02 mM); (c) Time-dependent degradation of FFA to detect $^1\text{O}_2$ ([FFA] = 0.02 mM); (d) Time-dependent degradation of NBT to detect $\text{}^{\cdot}\text{O}_2^-$ ([NBT] = 0.025 mM); (e) Accumulation of H_2O_2 . Experimental conditions: [*E. coli* K-12] = 2×10^7 cfu mL⁻¹, [Ag-AgBr/0.5% RGO] = 0.1 g L⁻¹.

et al., 2015b). Subsequently, $^{\circ}\text{O}_2^-$ undergoes facile disproportionation to produce $^{\circ}\text{OH}$, H_2O_2 and $^1\text{O}_2$ (Eqs. (3)–(6)) (Rengifo-Herrera et al., 2009; Castro et al., 2012). Moreover, such transportation of photogenerated electrons could also stabilize the photogenerated h^+ onto the surface of AgBr and Ag nanoparticles (Vatanssever et al., 2013). Although photogenerated h^+ on the VB_{AgBr} is thermodynamically forbidden to generate other ROSs, as the position of valence band (VB) in AgBr (+1.585 V vs NHE) is not positive enough to oxidize $\text{H}_2\text{O}/\text{OH}^-$ ($E_0(\text{OH}^{\cdot}/\text{OH}^-) = +2.38$ V vs NHE)) into $^{\circ}\text{OH}$ (Liu et al., 2015), the survived h^+ is still powerful enough to directly attack and oxidize the *E. coli* cells. Furthermore, attributed to this efficient electron transfer process, the excess electrons can be away from AgBr as far as possible, instead of reduction of silver ions in the AgBr, which ensures the stability of the Ag–AgBr/0.5% RGO. The generation procedures of RSs are shown in Eqs. (1)–(7), including e^- , h^+ , $^{\circ}\text{O}_2^-$, $^{\circ}\text{OH}$, $^1\text{O}_2$ and H_2O_2 , collectively contribute to the inactivation of *E. coli* K-12; and scavengers experiments reveal that the plasmon-induced H_2O_2 is the main reactive species in this photocatalytic inactivation process.



In conclusion, the antibacterial ability of Ag–AgBr/0.5% RGO originates from the synergistic activities of its three components, and the proposed mechanisms contain primary oxidative stress caused by plasmon-induced RSs as well as a minor bactericidal role of released Ag^+ ions.

3.4. Synergistic photocatalytic inactivation process of Ag–AgBr/0.5% RGO

From the aforementioned, Ag–AgBr/0.5% RGO was evidenced as a promising antimicrobial agent for water disinfection, in which plasmon induced RSs and released Ag^+ ions played a synergistic role. To further reveal and differentiate the inactivation mode of involved pathways of RSs and/or released Ag^+ ions, the bacterial inactivation process was analyzed by studying the change of cell morphology, cell metabolism, intracellular reactive oxidants, and cytoplasmic biomolecular during contacting with irradiated Ag–AgBr/0.5% RGO and Ag^+ ions.

The processed bacterial membrane integrity was visually observed by fluorescence microscopy as shown in Fig. 7(a1–c1). Notably, pure healthy *E. coli* K-12 cells with intact cell membrane exhibit brilliant green fluorescence (Fig. 7a1). With the addition of Ag–AgBr/0.5% RGO particles, the green color accumulates together, inferring some adsorption occurred between photocatalysts and cells. This result may explain the cells' loss after mixing with Ag–AgBr/0.5% RGO in dark control (Fig. 3b) were induced by the adsorption. After 10 min treatment, except for the yellow fluorescence emitted by Ag–AgBr/0.5% RGO, all the green fluorescence was replaced by red fluorescence, indicating cell membrane ruptured with prolonged irradiation time. Moreover, SEM test of

processed bacterial cells was also conducted and the images were shown in Fig. 7 (a2–e3), it can be seen that untreated *E. coli* cells (Fig. 7a2 and 7a3) display plump rod shapes with an intact cell envelope. With the addition of Ag–AgBr/0.5% RGO, *E. coli* and catalyst display great aggregation (Fig. 7b2 and 7b3), further confirming the efficient adsorption between *E. coli* and graphene domains. Previous reports mentioned that graphene sheet with broad conjugated sp^2 carbon network and large surface area can easily bind to the surface of microbial cells through the formation of lipopolysaccharide bridging (Liu et al., 2011; Castrillon et al., 2015). The enhanced bacterial adsorption by RGO is beneficial for promoting photocatalytic inactivation efficiency, because the concentrated cells over photocatalyst surface speed them to react with photogenerated active species. After 10 min treatment (Fig. 7c2 and c3), the surface of cells were wrinkled and became rougher, some even occupied by hollows and holes, indicating the extreme destruction of the cell envelope. In contrast, all the cells still emit green fluorescence when contacted with Ag–AgBr/0.5% RGO in dark (Fig. 7d1) or equivalent amount of released Ag^+ ions (Fig. 7e1), inferring the cell-membrane are still intact within the same experimental time period. Similarly, in SEM analysis, there are some rough wrinkles but no hollows can be observed on cell surface, indicating Ag^+ ions can only induce limited disruption of cell-membrane after 10 min treatment (Fig. 7e2 and 7e3). These results implied the mechanism of inactivation effect caused by Ag^+ ions are different from Ag–AgBr/0.5% RGO upon light irradiation, which cannot damage cell envelope seriously. This is plausible, as previous reports mentioned that dissolved Ag^+ ions can be easily captured and bounded by membrane associated proteins, then alert the natural permeability of cell membrane rather than direct oxidation like RSs, thereby rendered limited destruction in cell membrane (Kittler et al., 2010).

Obviously, results of microscopic study indicate that sustainably generated RSs can cause a myriad of adverse effects on the cell membrane. This may lead to the great damage of metabolic functions like ATP synthesis ability, because the essential enzyme of respiratory chain is mainly survived on the cell membrane. As shown in Fig. 8a, a rapid drop in the cellular ATP content (by 96%) with ATP level decrease from $285 \text{ RLU}/10^3$ to zero was observed following the exposure to VL irradiated Ag–AgBr/0.5% RGO within 10 min. The great generation of RSs could inhibit ATP formation by oxidizing or inhibiting enzymes like ATPase in the respiratory chain to dissipate the proton motive force of cell membrane and cause membrane dysfunction (Maness et al., 1999). In addition, the interaction between RSs with coupling enzymes (such as NADH and succinate dehydrogenase) also impedes the electron-shuttling process, causing the increased buildup of intracellular $^{\circ}\text{O}_2^-$ and H_2O_2 , further aggravate the destruction of cellular metabolized pathways (Xia et al., 2015b). Comparatively, light irradiation alone (light control) only cause negligible ATP inhibition, while dark control led to a 6.4% ATP inhibition (Fig. 8a). Moreover, the involvement of irradiated Ag^+ ions can cause about 12% ATP inhibition, indicating that the leaked Ag^+ ions play an independent ATP inhibition role under light irradiation (Fig. 8a). Ag^+ ions could be delivered to the inner cell and interact with thiols in enzymes, then results in a chain of events in the subsequent metabolic pathway, for example, inhibiting ATP formation by behaving like a protonophore or bind to coupling enzymes in the bacterial respiratory chain (bearing cysteine groups with a strong affinity to Ag^+ ions, such as NADH and succinate dehydrogenase) (Jung et al., 2008). Moreover, the presence of Ag^+ ions also enhances the susceptibility of the bacterial cells to ROS by depleting intracellular antioxidants such as glutathione (Park et al., 2009). Therefore, in the condition of VL irradiated Ag–AgBr/0.5%, it is clear to conclude that the presence of Ag^+ ions play a synergistic effect with RSs to inhibit the ATP

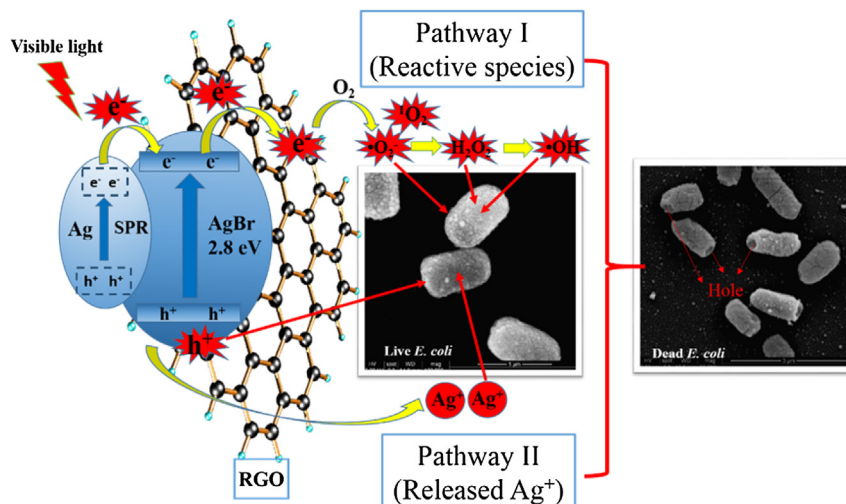


Fig. 6. Proposed synergistic photocatalytic bacterial inactivation mechanism by plasmonic Ag–AgBr/0.5% RGO composite photocatalyst.

formation.

To further reveal the bactericidal effect of photogenerated RSs and leaked Ag^+ ions, the widely-used fluorescent probe DCFH-DA was applied to analyze the formation of intracellular ROS with VL irradiated Ag–AgBr/0.5% RGO and Ag^+ ions. As shown in Fig. 8b, the levels of fluorescent intensity start to increase instantly in the initial 1 min with VL irradiated Ag–AgBr/0.5% RGO, mainly due to the instant penetration of diffusible $\cdot\text{OH}$ and H_2O_2 , as well as the induced buildup of $\cdot\text{O}_2^-$ and H_2O_2 through Fenton or Harber-Weiss reaction (Gogniat and Dukan, 2007); then sharply decrease within the following 5 min, indicating the great disruption of cellular antioxidative enzyme like superoxide dismutase (SOD) or catalase (CAT) and herewith fluorescent product leakage (Kikuchi et al., 1997). In contrast, only little increase of fluorescent intensity indicates limited RSs buildup in the presence of irradiated Ag^+ ions or dark control with Ag–AgBr/0.5% RGO (Fig. 8b). This observation suggests the minor role of Ag^+ ions in intracellular ROS formation, which is consistent with previous work (Loo et al., 2015). Harrison et al. (2009) also suggested that the bactericidal mechanism of Ag^+ ions was categorized as thiol-disulfide chemistry predominantly rather than ROS production, as Ag^+ ions can rapidly cause cellular thiol oxidation into metal disulfides and metal trisulfides involving little or no net ROS production.

Furthermore, the resultant ultra and intracellular ROS can subsequently injure the cells by reacting with various biomolecules. One possible route for ROS-mediated cell injury is the leakage and oxidation of the cellular protein, which was measured with Bradford assay. As shown in Fig. 8c, the protein content of 10 mL of treated cells was increased within the initial 3 min and maintained at around $160 \mu\text{g mL}^{-1}$ but then decreased a little to $138 \mu\text{g mL}^{-1}$ at 10 min, confirming the leakage and decomposition of protein during the treatment. However, no protein leakage happened in the presence of equivalent Ag^+ ions, this is plausible because the cells still maintain intact membranes in SEM and fluorescent microscopy studies. However, cellular extracted Ag^+ ions still can interact with thiols in proteins, bind to enzymes and even cause intracellular oxidative stress to proteins (Wigginton et al., 2010).

Besides the leakage and oxidation of cellular protein, the compromised cell envelope also induce the release and degradation of other cytoplasmic constituents such as DNA and RNA, can be monitored by their strong UV absorption at 260 nm (Liu et al., 2009). Only severe loss or damage of chromosomal DNA or RNA is lethal to the cells, or else cells still can self-repair and regrow

even when their proteins are damaged (Gogniat and Dukan, 2007). The optical density (OD) ratio of a bacterial suspension with irradiated Ag–AgBr/0.5% RGO of different irradiation period to its initial stage is plotted in Fig. 8d. This ratio shows a remarkable increment by a factor of 2.7 times at 3 min, then starts to decrease at 8 min after light irradiation, inferring the great leakage of DNA and RNA in the initial and followed by oxidation in the latter irradiation period. The results from this absorption study at 260 nm are in agreement with the inactivation kinetics in Fig. 3d, which shows almost 90% loss of bacterial mortality within the first 3 min and then total loss in the latter irradiation time. In contrast, as only negligible membrane destruction in the presence of Ag^+ ions was observed above, thereby no enhancement of UV absorption at 260 nm and limited leakage of DNA or RNA. However, it has been reported that the cellular extracted Ag^+ ions still can interact with phosphorus moieties of DNA, inactivating its replication process through preventing DNA from unwinding (Sun et al., 2016).

As a result, the disparity in the cell injury caused by Ag^+ ions versus that of Ag–AgBr/0.5% RGO (that show the combined effect of RSs and Ag^+ ions) can be clearly distinguished. These methods may resolve the debate over the disinfection mechanism of Ag-based plasmonic photocatalyst. The enhanced inactivation activities originated from the enhanced adsorption of graphene sheets, this process could facilitate the performance of the further inactivation effects which contained the following two pathways of Ag^+ ions and plasmonic induced RSs, as shown in Fig. 7: (I) free Ag^+ species released from Ag–AgBr/0.5% RGO bound to the cell membrane and enter intracellular environment resulting in metabolic dysfunction, and interruption of DNA replication; (II) plasmonic induced H_2O_2 plays the leading role, collaborating with e^- , $\cdot\text{O}_2^-$, $\cdot\text{OH}$, $^1\text{O}_2$, etc., to first degrade substances of cell envelope, then lead to the leakage and degradation of intracellular substances leakage.

4. Conclusions

In summary, Ag–AgX/RGO exhibited a great potential for water disinfection because of its efficient bactericidal effects under VL irradiation. The enhanced antimicrobial ability of irradiated Ag–AgBr/0.5% RGO is originated from the synergistic activities of its three components, and the proposed mechanisms contained chemical attraction of RGO, followed by bactericidal effect of released Ag^+ species and primary oxidative stress of plasmon e^- induced H_2O_2 , collectively lead to the damage of microbial

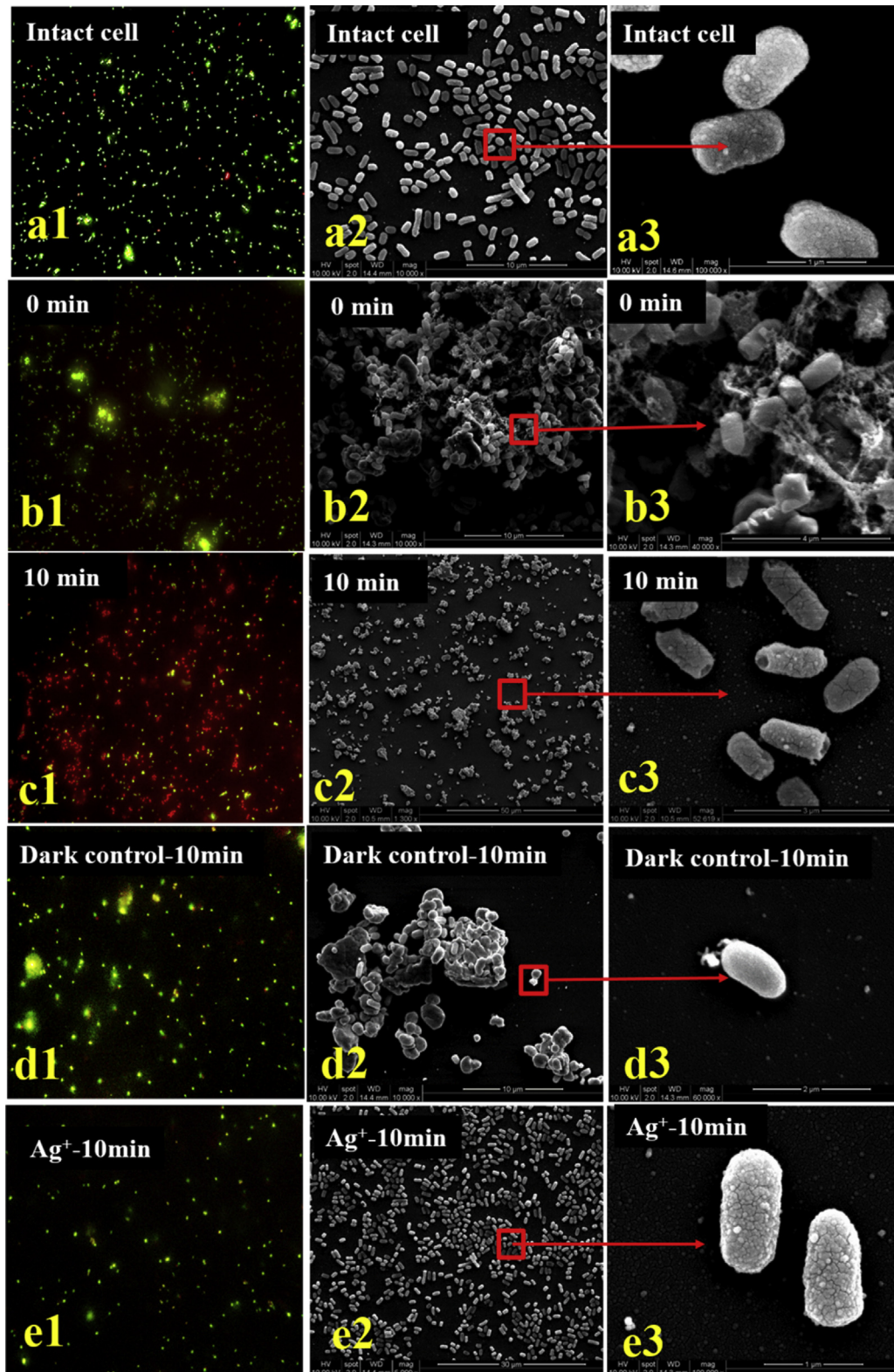


Fig. 7. Fluorescence microscopic images (a1–e1) and SEM images (a2–e3) of *E. coli* K-12: (a1–a3) untreated *E. coli* K-12, (b1–b3) before photocatalytic treatment with Ag/AgBr/0.5% RGO, (c1–c3) after photocatalytic treatment with Ag/AgBr/0.5% RGO for 10 min; (d1–d3) after mixture with Ag/AgBr/0.5% RGO in dark for 10 min; (e1–e3) after treatment with Ag⁺ ions for 10 min under light irradiation. Experimental conditions: [*E. coli* K-12] = 2×10^7 cfu mL⁻¹, [Ag/AgBr/0.5% RGO] = 0.1 g L⁻¹, [Ag⁺] = 0.58 mg L⁻¹.

metabolism processes and the destruction of cell envelope as well as leakage of intracellular substances. Especially, this work also systematically revealed the bactericidal role of released Ag⁺ ions,

which can induce the damage of metabolic process, but limited cell-membrane damage. Although most mechanistic studies reported herewith were based on Ag–AgBr/0.5% RGO, it is believed

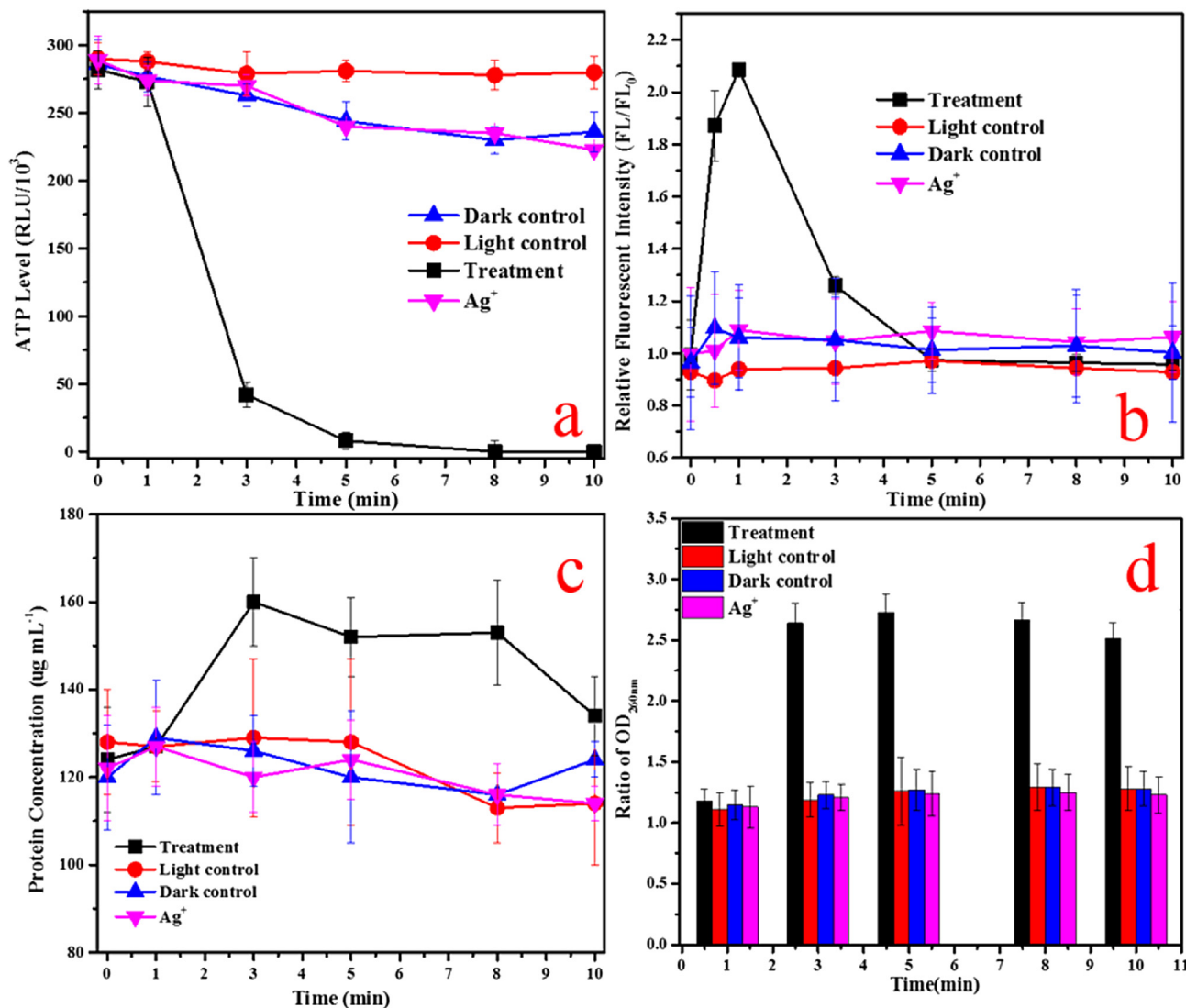


Fig. 8. (a) ATP content in cells (note: RLU denotes the relative luminescence unit); (b) Fluorescence measurement of intracellular ROS generation; (c) Degree of protein content leakage from the cells; (d) Degree of cytoplasmic content release from the cells (note: a higher OD_{260nm} indicates the release of more cytoplasmic contents). Experiment conditions: [Ag–AgBr/0.5% RGO] = 0.1 g L⁻¹, [Ag⁺] = 0.58 mg L⁻¹.

that the developed mechanistic understanding could be extended to other Ag based plasmonic photocatalysts. This study provides an efficient water disinfection technology and also opens a new idea in studying the antimicrobial mechanism of plasmonic photocatalyst.

Acknowledgement

The research project was supported by General Research Fund (GRF14100115) from Research Grant Council of Hong Kong SAR Government, and Technology and Business Development Fund (TBF15SCI008) of The Chinese University of Hong Kong to P.K. Wong, and National Natural Science Funds for Distinguished Young Scholars (41425015) and National Natural Science Foundation of China (41573086) to T.C. An and G.Y. Li Wong was also supported by the CAS/SAFEA International Partnership Program for Creative Research Teams of Chinese Academy of Sciences, China.

Appendix A. Supplementary data

Supplementary data related to this article can be found at <http://>

dx.doi.org/10.1016/j.watres.2016.04.055.

References

- Archana, P.S., Pachauri, N., Shan, Z., Pan, S., Gupta, A., 2015. Plasmonic enhancement of photoactivity by gold nanoparticles embedded in hematite films. *J. Phys. Chem. C* 119, 15506–15516.
- Bartusik, D., Aebischer, D., Lyons, A.M., Greer, A., 2012. Bacterial inactivation by a singlet oxygen bubbler: identifying factors controlling the toxicity of ¹O₂ bubbles. *Environ. Sci. Technol.* 46, 12098–12104.
- Castrillon, S.R.-V., Perreault, F., Faria, A.F., Elimelech, M., 2015. Interaction of graphene oxide with bacterial cell membranes: insights from force spectroscopy. *Environ. Sci. Technol. Lett.* 2, 112–117.
- Castro, C.A., Osorio, P., Sienkiewicz, A., Pulgarin, C., Centeno, A., Giraldo, S.A., 2012. Photocatalytic production of ¹O₂ and [•]OH mediated by silver oxidation during the photoinactivation of *Escherichia coli* with TiO₂. *J. Hazard. Mater.* 211–212, 172–181.
- Fabrega, J., Fawcett, S.R., Renshaw, J.C., Lead, J.R., 2009. Silver nanoparticle impact on bacterial growth: effect of pH, concentration, and organic matter. *Environ. Sci. Technol.* 43, 7285–7290.
- Gogniat, G., Dukan, S., 2007. TiO₂ photocatalysis causes DNA damage via Fenton reaction-generated hydroxyl radicals during the recovery period. *Appl. Environ. Microbiol.* 73, 7740–7743.
- Harrison, J.J., Tremaroli, V., Stan, M.A., Chan, C.S., Vacchi-Suzzi, C., Heyne, B.J., Parsek, M.R., Ceri, H., Turner, R.J., 2009. Chromosomal antioxidant genes have

- metal ion-specific roles as determinants of bacterial metal tolerance. *Environ. Microbiol.* 11, 2491–2509.
- Hu, X., Hu, C., Peng, T., Zhou, X., Qu, J., 2010. Plasmon-induced inactivation of enteric pathogenic microorganisms with Ag-AgI/Al₂O₃ under visible-light irradiation. *Environ. Sci. Technol.* 44, 7058–7062.
- Huang, J., Ho, W., Wang, X., 2014. Metal-free disinfection effects induced by graphitic carbon nitride polymers under visible light illumination. *Chem. Commun.* 50, 4338–4340.
- Jung, W.K., Koo, H.C., Kim, K.W., Shin, S., Kim, S.H., Park, Y.H., 2008. Antibacterial activity and mechanism of action of the silver ion in *Staphylococcus aureus* and *Escherichia coli*. *Appl. Environ. Microbiol.* 74, 2171–2178.
- Kittler, S., Greulich, C., Diendorf, J., Köller, M., Epple, M., 2010. Toxicity of silver nanoparticles increases during storage because of slow dissolution under release of silver ions. *Chem. Mater.* 22, 4548–4554.
- Kikuchi, Y., Sunada, K., Iyoda, T., Hashimoto, K., Fujishima, A., 1997. Photocatalytic bactericidal effect of TiO₂ thin films: dynamic view of the active oxygen species responsible for the effect. *J. Photochem. Photobiol. A Chem.* 106, 51–56.
- Kuai, L., Geng, B., Chen, X., Zhao, Y., Luo, Y., 2010. Facile subsequently light-induced route to highly efficient and stable sunlight-driven Ag-AgBr plasmonic photocatalyst. *Langmuir* 26, 18723–18727.
- Lan, Y., Hu, C., Hu, X., Qu, J., 2007. Efficient destruction of pathogenic bacteria with AgBr/TiO₂ under visible light irradiation. *Appl. Catal. B Environ.* 73, 354–360.
- Li, G., Nie, X., Chen, J., Jiang, Q., An, T., Wong, P.K., Zhang, H., Zhao, H., Yamashita, H., 2016. Enhanced visible-light-driven photocatalytic inactivation of *Escherichia coli* using g-C₃N₄/TiO₂ hybrid photocatalyst synthesized using a hydrothermal-calcination approach. *Water Res.* 86, 17–24.
- Li, Y., Zhang, H., Liu, P., Wang, D., Li, Y., Zhao, H., 2013. Cross-linked g-C₃N₄/rGO nanocomposites with tunable band structure and enhanced visible light photocatalytic activity. *Small* 9, 3336–3344.
- Lin, Q., Guo, B., Yu, J., Ran, J., Zhang, B., Yan, H., Gong, J., 2011. Highly efficient visible-light-driven photocatalytic hydrogen production of CdS-cluster-decorated graphene nanosheets. *J. Am. Chem. Soc.* 133, 10878–10884.
- Liu, S., Wei, L., Hao, L., Fang, N., Chang, M.W., Xu, R., Yang, Y., Chen, Y., 2009. Sharper and faster “nano darts” kill more bacteria: a study of antibacterial activity of individually dispersed pristine single-walled carbon nanotube. *ACS Nano* 3, 3891–3902.
- Liu, S., Zeng, T.H., Hofmann, M., Burcombe, E., Wei, J., Jiang, R., Kong, J., Chen, Y., 2011. Antibacterial activity of graphite, graphite oxide, graphene oxide, and reduced graphene oxide: membrane and oxidative stress. *ACS Nano* 9, 6971–6980.
- Liu, Z., Guo, W., Guo, C., Liu, S., 2015. Fabrication of AgBr nanomaterial as excellent antibacterial agents. *RSC Adv.* 5, 72872–72880.
- Loo, S.-L., Krantz, W.B., Fane, A.G., Gao, Y., Lim, T.-T., Hu, X., 2015. Bactericidal mechanisms revealed for rapid water disinfection by superabsorbent cryogels decorated with silver nanoparticles. *Environ. Sci. Technol.* 49, 2310–2318.
- Luo, G., Jiang, X., Li, M., Shen, Q., Zhang, L., Yu, H., 2013. Facile fabrication and enhanced photocatalytic performance of Ag/AgCl/rGO heterostructure photocatalyst. *ACS Appl. Mater. Interf.* 5, 2161–2168.
- Maness, P.-C., Smolinski, S., Blake, D.M., Huang, Z., Wolfrum, E.J., Jacoby, W.A., 1999. Bactericidal activity of photocatalytic TiO₂ reaction: toward an understanding of its killing mechanism. *Appl. Environ. Microbiol.* 65, 4094–4098.
- McEvoy, J.G., Zhang, Z., 2014. Synthesis and characterization of magnetically separable Ag/AgCl-magnetic activated carbon composites for visible light induced photocatalytic detoxification and disinfection. *Appl. Catal. B Environ.* 160–161, 267–278.
- Meng, X., Shao, X., Li, H., Yin, J., Wang, J., Liu, F., Liu, X., Wang, M., Zhong, H., 2013. Ag/AgBr/rGO nanocomposites: synthesis and its application in photocatalysis. *Mater. Lett.* 105, 162–165.
- Ng, T.W., An, T., Li, G., Ho, W.K., Yip, H.Y., Zhao, H., Wong, P.K., 2015. The role and synergistic effect of the light irradiation and H₂O₂ in photocatalytic inactivation of *Escherichia coli*. *J. Photochem. Photobiol. B Biol.* 149, 164–171.
- Pang, M., Hu, J., Zeng, H.C., 2010. Synthesis, morphological control, and antibacterial properties of hollow/solid Ag₂S/Ag heterodimers. *J. Am. Chem. Soc.* 132, 10771–10785.
- Park, H.-J., Kim, J.Y., Kim, J., Lee, J.-H., Hahn, J.-S., Gu, M.B., Yoon, J., 2009. Silver-ion-mediated reactive oxygen species generation affecting bactericidal activity. *Water Res.* 43, 1027–1032.
- Planas, O., Macia, N., Agut, M., Nonell, S., Heyne, B., 2016. Distance-dependent plasmon-enhanced singlet oxygen production and emission for bacterial inactivation. *J. Am. Chem. Soc.* 138, 2762–2768.
- Qu, X., Alvarez, P.J.J., Li, Q., 2013. Applications of nanotechnology in water and wastewater treatment. *Water Res.* 47, 3931–3946.
- Rengifo-Herrera, J.A., Pierzchała, K., Sienkiewicz, A., Forró, L., Kiwi, J., Pulgarin, C., 2009. Abatement of organics and *Escherichia coli* by N, S co-doped TiO₂ under UV and visible light. Implications of the formation of singlet oxygen (¹O₂) under visible light. *Appl. Catal. B Environ.* 88, 398–406.
- Rizzello, L., Pompa, P.P., 2014. Nanosilver-based antibacterial drugs and devices: mechanisms, methodological drawbacks, and guidelines. *Chem. Soc. Rev.* 43, 1501–1518.
- Shannon, M.A., Bohn, P.W., Elimelech, M., Georgiadis, J.G., Marinas, B.J., Mayes, A.M., 2008. Science and technology for water purification in the coming decades. *Nature* 452, 301–310.
- Shi, H., Chen, J., Li, G., Nie, X., Zhao, H., Wong, P.K., An, T., 2013. Synthesis and characterization of novel plasmonic Ag/AgX-CNTs (X = Cl, Br, I) nanocomposite photocatalysts and synergetic degradation of organic pollutant under visible light. *ACS Appl. Mater. Interf.* 5, 6959–6967.
- Shi, H., Li, G., Sun, H., An, T., Zhao, H., Wong, P.K., 2014. Visible-light-driven photocatalytic inactivation of *E. coli* by Ag/AgX-CNTs (X = Cl, Br, I) plasmonic photocatalysts: bacterial performance and deactivation mechanism. *Appl. Catal. B Environ.* 158–159, 301–307.
- Sun, H., Li, G., Nie, X., Shi, H., Wong, P.K., Zhao, H., An, T., 2014. Systematic approach to in-depth understanding of photoelectrocatalytic bacterial inactivation mechanisms by tracking the decomposed building blocks. *Environ. Sci. Technol.* 48, 9412–9419.
- Sun, H., Li, G., An, T., Zhao, H., Wong, P.K., 2016. Unveiling the photoelectrocatalytic inactivation mechanism of *E. coli*: convincing evidence from responses of parent and anti-oxidation single gene knockout mutants. *Water Res.* 88, 135–143.
- Vatansver, F., de Melo, W.C., Avci, P., Vecchio, D., Sadasivam, M., Gupta, A., Chandran, R., Karimi, M., Parizotto, N.A., Yin, R., Tegos, G.P., Hamblin, M.R., 2013. Antimicrobial strategies centered around reactive oxygen species- bactericidal antibiotics, photodynamic therapy, and beyond. *FEMS Microbiol. Rev.* 37, 955–989.
- Wang, J., An, C., Liu, J., Xi, G., Jiang, W., Wang, S., Zhang, Q., 2013a. Graphene oxide coupled AgBr nanosheets: an efficient dual-functional visible-light-responsive nanophotocatalyst with enhanced performance. *J. Mater. Chem. A* 1, 2827–2832.
- Wang, W., Yu, J.C., Xia, D., Wong, P.K., Li, Y.C., 2013b. Graphene and g-C₃N₄ nanosheets wrapped elemental α-Sulfur as a novel metal-free heterojunction photocatalyst for bacterial inactivation under visible-light. *Environ. Sci. Technol.* 47, 8724–8732.
- Wigginton, N.S., Titta, A.D., Picciapetra, F., Dobias, J., Nesatyy, V.J., Suter, M.J.F., Bernier-Latmani, R., 2010. Binding of silver nanoparticles to bacterial proteins depends on surface modifications and inhibits enzymatic activity. *Environ. Sci. Technol.* 44, 2163–2168.
- World Health Organization (WHO), 2008. World Health Organization: Volume Guidelines for Drinking-water Quality, third ed. (Geneva).
- Xi, B., Chu, X., Hu, J., Bhatia, C.S., Danner, A.J., Yang, H., 2014. Preparation of Ag/TiO₂/SiO₂ films via photo-assisted deposition and adsorptive self-assembly for catalytic bactericidal application. *Appl. Surf. Sci.* 311, 582–592.
- Xia, D., Li, Y., Fong, C.C., Huang, G., An, T., Li, G., Yip, H.Y., Zhao, H., Lu, A., Wong, P.K., 2015a. Elevating visible-light-driven photocatalytic inactivation of *Escherichia coli* K-12 using magnetic natural pyrrhotite minerals as photocatalyst by thermal treatment. *Appl. Catal. B Environ.* 176–177, 749–756.
- Xia, D., Shen, Z., Huang, G., Wang, W., Yu, J., Wong, P.K., 2015b. Red phosphorus: an earth-abundant elemental photocatalyst for “green” bacterial inactivation under visible light. *Environ. Sci. Technol.* 49, 6264–6273.
- Xia, D., Hu, L., Tan, X., He, C., Pan, W., Yang, T., Huang, Y., Shu, D., 2016. Immobilization of self-stabilized plasmonic Ag-AgI on mesoporous Al₂O₃ for efficient purification of industrial waste gas with indoor LED illumination. *Appl. Catal. B Environ.* 185, 295–306.
- Xia, D., Ng, T.W., An, T., Li, G., Li, Y., Yip, H.Y., Zhao, H., Lu, A., Wong, P.K., 2013. A recyclable mineral catalyst for visible-light-driven photocatalytic inactivation of bacteria: natural magnetic sphalerite. *Environ. Sci. Technol.* 47, 11166–11173.
- Xiu, Z., Liu, Y., Mathieu, J., Wang, J., Zhu, D., Alvarez, P.J.J., 2014. Elucidating the genetic basis for *Escherichia coli* defense against silver toxicity using mutant arrays. *Environ. Toxicol. Chem.* 33, 993–997.
- Yao, K., Wang, D., Yan, J., Yang, L., Chen, W., 2007. Photocatalytic effects of TiO₂/Fe thin film irradiated with visible light on cellular surface ultrastructure and genomic DNA of bacteria. *Surf. Coat. Technol.* 201, 6882–6885.
- Yu, J.C., Gkeiho, W., Yu, J., Yip, H.Y., Wong, P.K., Zhao, J., 2005. Efficient visible-light-induced photocatalytic disinfection on sulfur-doped nanocrystalline titania. *Environ. Sci. Technol.* 39, 1175–1179.
- Zhang, H., Fan, X., Quan, X., Chen, S., Yu, H., 2011. Graphene sheets grafted Ag@AgCl hybrid with enhanced plasmonic photocatalytic activity under visible light. *Environ. Sci. Technol.* 45, 5731–5736.
- Zhang, L., Wong, P.-K., Yip, H.-Y., Hu, C., Yu, J., Chan, C., Wong, P.K., 2010. Effective photocatalytic disinfection of *E. coli* K-12 using AgBr-Ag-Bi₂WO₆ nanojunction system irradiated by visible light: the role of diffusing hydroxyl radicals. *Environ. Sci. Technol.* 44, 1392–1398.
- Zhao, W., Li, J., Wei, Z., Wang, S., He, H., Sun, C., Yang, S., 2015. Fabrication of a ternary plasmonic photocatalyst of Ag/AgVO₃/RGO and its excellent visible-light photocatalytic activity. *Appl. Catal. B Environ.* 179, 9–20.
- Zhu, M., Chen, P., Liu, M., 2011. Graphene oxide wrapped Ag/AgX (X = Br, Cl) nanocomposites as a highly efficient visible-light plasmonic photocatalyst. *ACS Nano* 5, 4529–4536.
- Zhu, M., Chen, P., Liu, M., 2012. Ag/AgBr/graphene oxide nanocomposite synthesized via oil/water and water/oil microemulsions: a comparison of sunlight energized plasmonic photocatalytic activity. *Langmuir* 28, 3385–3390.